Accepted Manuscript

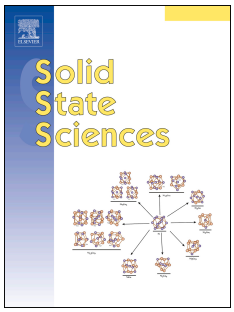

Effect of Tb^{3+} concentration in the visible emission of terbium-doped gadolinium oxysulfide microspheres

Luis Hernandez-Adame, Gabriela Palestino, Octavio Meza, Pablo Luis Hernandez-Adame, Hector Rene Vega-Carrillo, Iyad Sarhid

PII: S1293-2558(18)30396-0

DOI: 10.1016/j.solidstatesciences.2018.07.021

Reference: SSSCIE 5737

To appear in: *Solid State Sciences*

Received Date: 5 April 2018

Revised Date: 30 July 2018

Accepted Date: 31 July 2018

Please cite this article as: L. Hernandez-Adame, G. Palestino, O. Meza, P.L. Hernandez-Adame, H.R. Vega-Carrillo, I. Sarhid, Effect of Tb^{3+} concentration in the visible emission of terbium-doped gadolinium oxysulfide microspheres, *Solid State Sciences* (2018), doi: 10.1016/j.solidstatesciences.2018.07.021.

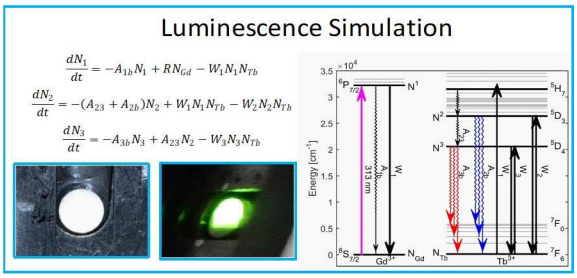

Effect of Tb^{3+} Concentration in the Visible Emission of Terbium-doped Gadolinium Oxysulfide Microspheres

Luis Hernandez-Adame[1*], Gabriela Palestino[2], Octavio Meza[3], Pablo Luis Hernandez-Adame[4], Hector Rene Vega-Carrillo[5] and Iyad Sarhid[6]

[1]CONACyT-Centro de Investigaciones Biológicas del Noroeste (CIBNOR), Instituto Politécnico Nacional 195, Playa Palo de Santa Rita Sur, La Paz, B.C.S. 23090 Mexico.

[2]Biopolymers and Nanostructures Laboratory, Faculty of Chemical Sciences, Universidad Autónoma de San Luis Potosí, Av. Manuel Nava No. 6, San Luis Potosí, S.L.P. 78210, Mexico.

[3]Instituto de Física, Benemérita Universidad Autónoma de Puebla, Apdo, Postal J-48, Puebla, Pue., C.P. 72570, Mexico.

[4]Colloids and Interfaces Laboratory, Institute of Physics, Universidad Autónoma de San Luis Potosí, Av. Manuel Nava No. 6, San Luis Potosí, S.L.P., 78210, Mexico.

[5]Universidad Autonoma de Zacatecas, UA de Estudios Nucleares, Cipres 10, Fracc. La Peñuela, Zacatecas, Zac., 98060, Mexico.

[6]Laboratoire de Chimie Physique, UMR 8000 CNRS, Université Paris-Sud, Université Paris-Saclay, Orsay, 91405, France.

*Corresponding author.

Address: CONACyT- Centro de Investigaciones Biológicas del Noroeste (CIBNOR), Instituto Politécnico Nacional 195, Playa Palo de Santa Rita Sur, La Paz, B.C.S. 23090 Mexico.

Tel: 01 612-1238484 ext. 3344

E-mail address: ladame@cibnor.mx

Abstract

Experimental data obtained from optical characterization of $Gd_2O_2S:Tb^{3+}$ microspheres were compared with a rate-equation model in order to understand and simulate the emission intensity and color tonality as a function of Tb^{3+} concentration. The microparticles were prepared by hydrothermal synthesis and characterized by TEM and XRD to confirm spherical microparticles with a hexagonal lattice. Furthermore, fluorescent spectroscopy and rate equation model revealed that the direct energy transfer between $Gd^{3+} \rightarrow Tb^{3+}$ ions and the migration of the excitation energy between Tb^{3+} play an important role in the luminescence intensity, while the

color tonality is mainly governed by the non-radiative relaxation processes between Tb^{3+} at low concentrations. Finally, our results suggest that the rate equation model provides an efficient alternative to estimate theoretically the maximum doping concentration in oxysulfides before they present quenching of luminescence.

Keywords: gadolinium oxysulfide; rate equations; luminescence simulation; microspheres.

1. Introduction

Nowadays, there is an ongoing search for developing luminescent materials to be used in biomedical and technological applications [1–4]. For this, inorganic compounds such as oxides and oxysulfides are doped with rare earth ions (Y_2O_3, ZnO, ZrO_2, Gd_2O_3, and Gd_2O_2S) and have shown excellent results. In particular, the gadolinium oxysulfide (Gd_2O_2S) that has shown interesting properties such as high chemical and thermal stability, wide band gap, and excellent electronic mobility that make it as one of the first candidates for developing new platforms for magnetic resonance, X-ray and photoluminescence imaging [5–8]. Regarding its synthesis, in our previous work, we presented results referring to the production of terbium activated gadolinium oxysulfide ($Gd_2O_2S:Tb^{3+}$) with specific size and shape. Also, we proposed a methodology of facile-doping Gd_2O_2S host lattice with different concentrations of rare earth ions to increase emission intensity [9]. The emission spectrum of Gd_2O_2S consists of well-defined peaks in the UV and visible region, of which, peaks from 413 to 679 nm are the most intense with a main emission band at 544 nm. This emission band correlates with the observable green emission under UV excitation. The mechanism involving this visible emission is an efficient non-radiative energy transfer from Gd^{3+} to Tb^{3+} ions because the electronic configuration of Gd^{3+} does not have a direct emission in the visible region from its own populated energy levels. This experimental evidence has been sufficient to explain the emission and intensity at 544 nm, however, the ratio between peaks that define the color tonality from red to blue as a function of Tb^{3+} concentration, is not clear and also needs to be understood [10–12].

In this sense, in order to understand and simulate the emission intensity and color tonality as a function of Tb^{3+} concentration in $Gd_2O_2S:Tb^{3+}$ microcrystals, we present

a set of algebraic equations that sufficiently explains the luminescent behavior under 313 nm excitation. Our comparison between experimental and theoretical results demonstrate a direct energy transfer between $Gd^{3+} \rightarrow Tb^{3+}$ ions and reveals that the concentration and migration of the excitation energy in the Tb^{3+} play an important role in the luminescence intensity, while the color tonality is mainly governed by non-radiative relaxation processes between the same ions at low concentrations. Finally, this model can estimate theoretically the maximum doping concentration in the Gd_2O_2S matrix before the quenching of luminescence occurs, as well as, the energy transfer processes between Gd and Tb ions into this lattice.

2. Experimental

All reagents were purchased from Sigma Aldrich (99.99 %) and used without further purification process. Gadolinium nitrate and Terbium nitrate used as precursors, urea as a precipitate agent, and ultra-purified Mili-Q water (18.5 MΩ) for washing and preparing all the solutions.

The Gd_2O_2S:Tb microspheres were prepared by using the urea precipitation method and sulfur vaporization according to our previous report [9]. The synthesis is divided into three stages: 1) growth of the rare earth hydroxycarbonates ($Gd(OH)CO_3 \bullet H_2O$:Tb), 2) oxidation process (Gd_2O_3:Tb), and 3) production of Gd_2O_2S:Tb by a sulfidation reaction.

The synthesis of the rare earth hydroxycarbonates is a key step to obtain the shape and size of the particle. This process is induced by urea decomposition at high temperature that promotes the controlled release of carbonate groups (CO_3^{2-}) that form a complex with the lanthanide ions weakly hydrolyzed and causes the precipitation once the critical supersaturation is achieved. The temperature, reaction time, and molar ratio of urea and lanthanides in the solution determines the shape and mean particle size [9]. This stage was carried out as follows; in a round bottom flask, a 150 mL aqueous solution with $Gd(NO_3)_3 \bullet 6H_2O$ and $Tb(NO_3)_3 \bullet 6H_2O$ (15 mM of total concentration) was heated to 60 °C for 15 min under magnetic stirring. Later, a 150 mL aqueous solution with urea (50 mM) was added to the first solution with a volumetric rate of 3 ml/min under vigorous stirring. The temperature of the new 300 mL aqueous solution was increased up to 85 °C and the reaction was carried out for an aging time of 1.5 h. At this point, the transparent solution turned blue-white, which

indicates the formation of $Gd(OH)CO_3•H_2O$ microparticles due to the complexation of carbonate groups with the metallic cations (Gd and Tb). The solution was left to cool down naturally to room temperature, and the precipitate was separated by centrifugation (6000 rpm/5 min), washed four times with deionized water and dried in an oven at 100 °C for 12 h to finally obtain the freshly prepared $Gd(OH)CO_3$:Tb powders.

The oxidation process was achieved by calcination of the $Gd(OH)CO_3$:Tb powders. The reaction was carried out in a furnace at 800 °C for 2 h to eliminate the organic precursors and produce the gadolinium oxide doped by terbium ($Gd_2O_3:Tb^{3+}$).

Finally, the $Gd_2O_2S:Tb^{3+}$ samples were prepared through sulfidation reaction that was carried out in a two-holder quartz reactor. Here, the first holder was used as a reservoir for sulfur powders, and the second for placing the freshly prepared $Gd_2O_3:Tb^{3+}$. The section of reactor that contain the $Gd_2O_3:Tb^{3+}$ was introduced into a tubular furnace, while the first holder was left at the inlet of the furnace, wrapped it with an electrical heating appliance and then heated at 350 °C to obtain sulfur gas, which was brought through the whole system by high purity nitrogen used as a gas carrier. The sulfidation reaction was produced by annealing the oxide to 900 °C for 3 h under the sulfur-nitrogen gas stream. After reaction time, the sample was cooled down to room temperature, maintaining the N_2 flow throughout the system. A representative diagram of the sulfidation set up, is shown in Figure S2.

In order to analyze the influence of Tb^{3+} concentration, a set of $Gd_2O_2S:Tb^{3+}$ powders with different dopant concentrations (0.01, 0.1, 1.5, 3, and 9 % mol) were prepared. The samples were labeled as GOS0.01, GOS0.1, GOS1.5 GOS3 and GOS9 that correspond to each sample with its Tb^{3+} content, respectively. The dopant content was calculated on mol percent as follows: $Gd^{3+}:Tb^{3+} = X:(1 - X)$ and $X + Y = 1$, where X is the molar fraction of Gd^{3+} and Y is the molar fraction of Tb^{3+}. A summary of all samples with their calculated and real Tb^{3+} content determined by ICP-OES, is given in Table I.

Table I. Set of $Gd_2O_2S:Tb^{3+}$ samples with their calculated and real Tb^{3+} content determined by ICP-OES.

Sample	Calculated Gd content [% mol]	Calculated Tb content [% mol]	Real Tb content by ICP-OES [% mol]	Nanoparticles		Figure
				Shape	Size [nm]	
GOS0.01	99.99	0.01	0.0084	Sphere	100±15	2a
GOS0.1	99.9	0.1	0.083	Sphere	102±5	2b
GOS1.5	98.5	1.5	1.26	Sphere	125±9	2c
GOS3	97	3	2.52	Sphere	115±31	2d
GOS9	91	9	7.56	Sphere	122±28	2e

2.1 Characterization

Crystallography was analyzed by Wide Angle X-ray Diffraction (WAXD) using a PANalytical model Xpert pro. The powders were illuminated with $CuK\alpha_1$ (λ=1.5418 Å) X-rays and the diffractograms were recorded in the range of 20–70° (2θ). The morphology and particle size were measured by Transmission Electron Microscopy (TEM) in a Joel Jem 1230 operated at 200 kV. The Fluorescence spectroscopy was analyzed in a Horiba Join-Yvon spectrometer. The samples were prepared by forming a pellet produced by applying 3 tons of pressure on 10 mg of powders for 25 min. The pellet was placed on the solid holder, mounted at 45° in relation to the incident beam. The elemental analysis and doping content were analyzed by using the ICP-OES technique with an Ultimate 2 Horiba system. Here, the sample was prepared by digesting 80 mg of powder using a 1:3 $HCl:H_2O$ mixture (12 $M:H_2O$ deionized).

3. Results and discussion

3.1 Crystallography

The XRD patterns of $Gd_2O_2S:Tb^{3+}$ microcrystals with different Tb^{3+} content are shown in Figure 1. Here, it is important to note that all samples show the same diffraction peaks (101), (100), (102), (003), etc, corresponding to the hexagonal phase of Gd_2O_2S (space group P-3m1 and JCPDS 26-1422). This observation suggests that Tb ions are being introduced into the Gd_2O_2S matrix regardless of doping concentrations. This effect is possible because Tb ions have a slightly lower

ionic radius (1.77 Å) than Gd ones (1.79 Å), so they can occupy the same sites within the crystalline lattice. Furthermore, XRD patterns also show a slight shift to larger angles in all diffraction peaks. The largest change was observed by the sample GOS09 that contains the highest dopant content (9 %mol). Here, the planes 101 and 100 show a slight shift of +0.34° compared with the same planes of the reference card. This effect is due to a small contraction of the crystal structure produced by the incorporation of ions with smaller ionic radii. Moreover, we estimated the lattice parameter using the two principal peaks ((100) and (102)) with the equation 1 and were compared with the obtained by Rietveld refinement for each sample [13]. The resulting calculated parameters are shown in Table II and Table 1S. Details of the calculations can be found in the appendices 3.1 of the supporting information. In addition, due to the cell parameters obtained by both methods are so quite similar, for further calculations, we decide to use the parameters obtained by the equation 1 due to its simplicity and the adjustment that it has with the experimental diffractograms.

$$\frac{4sin(\theta)^2}{L^2} = \frac{4}{3}\left(\frac{h^2}{a^2} + \frac{hk}{a^2} + \frac{k^2}{a^2}\right) + \frac{l}{c^2} \quad (1)$$

It is important to note that N_{Tb} value obtained for the sample GOS3 (3%mol) by using the ICP-OES technique, reached a real Tb^{3+} incorporation of 2.52 %mol (~84% efficiency) (see Table I). This indicates that we have a real N_{Tb} of (5.72 ± 1.2) $x10^{20}$ atoms of Tb^{+3}/cm^3 instead of 6.824 $x10^{20}$ atoms of Tb^{+3}/cm^3 calculated for the same sample. Due to this estimation has a significant deviation, for practical purposes we used the real N_{Tb} values of all samples (see Table II) to solve the rate equation model proposed in section 3.4. This N_{Tb} value is important in our study, due to that the amount of Tb^{3+} ions, will play an important role in the radiative versus non-radiative decay mechanisms [10,14,15]; these electronic transitions define the position of the emission lines and the ratio between them, and can be strongly affected by the interionic distances and crystalline symmetry properties [16,17]. Due to all samples have the same hexagonal phase, it is possible to study the optical properties as a function of the dopant concentration [18].

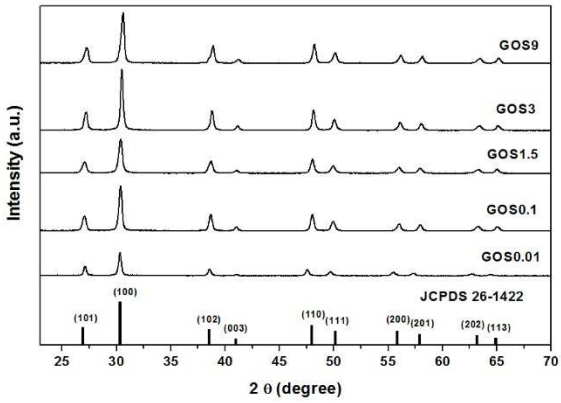

Figure 1. Diffractograms of $Gd_2O_2S:Tb^{3+}$ with different Tb^{3+} content calcined at 900 °C. The patterns correspond to GOS0.01, GOS0.1, GOS1.5, GOS3 and GOS9 samples, respectively.

Table II. Unit cell parameters of $Gd_2O_2S:Tb^{3+}$ samples belonging to space group P-3m1 with their nominal Tb^{3+} amount (N_{Tb}) [ions/cm^3], respectively.

Sample	unit cell parameters			Calculated N_{Tb} ions/cm^3 [1x10^{20}]	Real N_{Tb} ions/cm^3 [1x10^{20}]
	a [Å]	c [Å]	V [Å^3]		
GOS0.01	3.8288	6.9964	88.8196	0.0234	0.01965
GOS0.1	3.8094	6.9965	87.9256	0.2361	0.1983
GOS1.5	3.7679	6.9966	86.0230	3.4874	2.9294
GOS3	3.7390	6.9969	85.2886	6.8240	5.7221
GOS9	3.7518	6.9965	84.7112	20.2658	17.0232

3.2 Morphology

Shape and size distribution of all samples are shown in Figures 2 and S1, respectively. Here, the TEM images demonstrate microparticles well dispersed with a spherical shape and an average size of a) 100±15, b) 102±5, c) 125±9, d) 115±31, and e) 122±28 nm, respectively (see Table II and S1). Since the size distribution of all samples is ranging in the same order of magnitude; we wouldn't expect to obtain a significant influence on the luminescent emission due to the particle size variation.

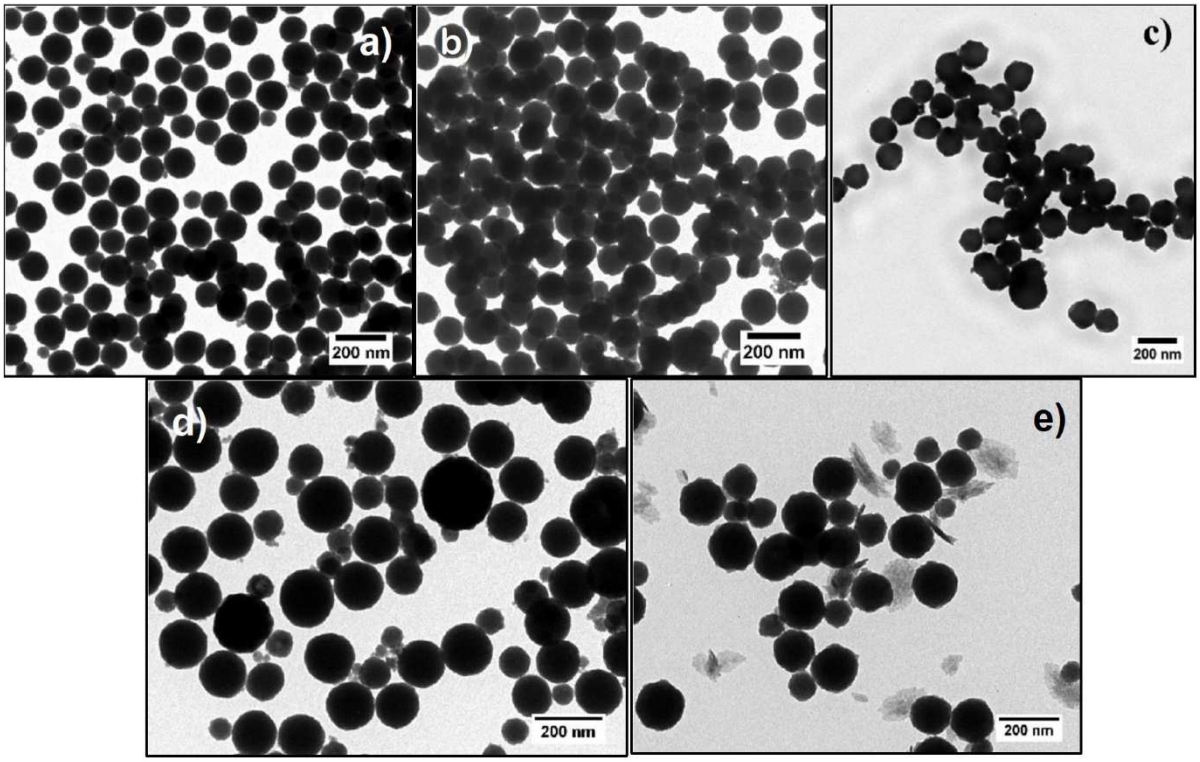

Figure 2. $Gd_2O_2S:Tb^{3+}$ spherical microparticles with 0.01(a), 0.1(b), 1.5(c), 3(d) and 9(c) % mol of Tb^{3+} concentration.

3.3 Photoluminescence and concentration quenching

Under 313 nm excitation, the crystals of $Gd_2O_2S:Tb^{3+}$ present VIS luminescence, as shown in the emission spectra of Figure 3. These processes can be described according to the Gd^{3+} and Tb^{3+} energy levels (see Figure 4), and the mechanisms can be explained as follows: Firstly, the Gd^{3+} ions are excited from the ground state $^8S_{7/2}$ up to the excited state $^6P_{7/2,}$ subsequently, some excited Gd^{3+} ions in $^6P_{7/2}$ state can transfer their energy to ions of Tb^{3+} in the ground state $^7F_6$ and populate the $^5H_7$ energy level, Gd^{3+} ($^6P_{7/2}$, $^8S_{7/2}$) → Tb^{3+} ($^7F_{6,}{}^5H_7$). The populated $^5H_7$ state rapidly relaxes to $^5D_3$ energy level, which produces downshift violet-blue luminescence, between 360 and 460 nm. In Figure 3, the most prominent emission is around 475 to 600 nm, which is produced by radiative transitions from $^5D_4$ level [11]. One can conclude, that a bigger part of the electronic population at level $^5D_3$ relaxes nonradiatively to the lower $^5D_4$ level. Figure 5 shows the integrated radiative emission of $^5D_3$ (N_2) and $^5D_4$ (N_3) energy levels. In both cases, the emission intensity has

fluctuated as a function of the Tb^{3+} concentration. This effect is called concentration quenching of luminescence [16,17,19].

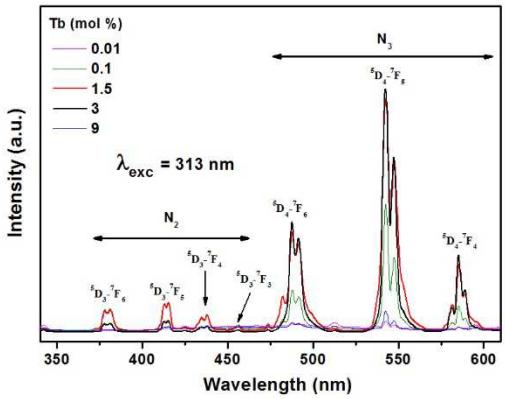

Figure 3. Emission fluorescence spectra of the Gd_2O_2S crystals doped with different Tb^{3+} concentrations upon an excitation at 313 nm.

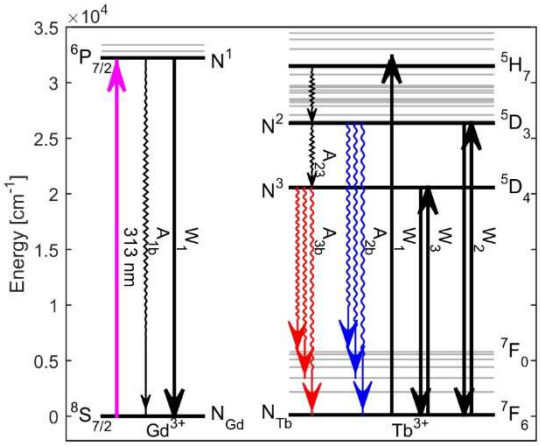

Figure 4. Schematic energy-level diagram showing the downshifting mechanism (Blue and red arrows) and the Interionic non-radiative transitions (Black arrows) in microspheres of $Gd_2O_2S:Tb^{3+}$.

In principle, an increase in the concentration of a luminescent center, in a given material, should be accompanied by an increase in the emitted light intensity. However, such behavior only occurs up to a certain critical concentration of the luminescent centers. Above this concentration, the luminescent intensity starts to decrease. In general, the origin of concentration quenching of luminescence, lies in a very efficient energy transfer among the luminescent centers. Two mechanisms are generally invoked to explain the luminescence concentration quenching: (1)

Quenching trap mechanism and 2) cross relaxation mechanism [20]. (1) The quenching trap mechanism is due to a very efficient energy transfer, the excitation energy of Tb^{3+} ions can migrate through a large number of Tb^{3+} ions before being emitted. However, even for the purest crystals, there is always a certain concentration of defects, or trace ions that can act as acceptors. These centers can relax to their ground state by multiphonon route instead of radiative emission, and the effect is perceived as the reduction of luminescence as shown the Figure 5. (2). At a certain concentration, quenching can also be produced without actual migration of the excitation energy among the luminescent centers. This occurs when the excitation energy is lost from the emitting state, via cross-relaxation mechanism, $Tb^{3+}(^5D_3,^5D_4) \rightarrow Tb^{3+}(^7F_0,\ ^7F_6)$. This mechanism decreases the emission $^5D_3$ level by increasing Tb^{3+} concentration (see Figure 5a). However, the nature of the process, in principle, also increase the emission of the $^5D_4$ level by increasing Tb^{3+} concentration, but such behavior does not agree with experimental reality (see Figure 5b), for Tb^{3+} concentrations higher than 1.5 mol%, the emission in both bands decrease with Tb^{3+} concentration. In this way, the quenching trap mechanism by migration of energy must be important [21, 22], and this process in general decrease the emission. Due to these arguments, in our model, we consider only the quenching traps mechanism and not the cross-relaxation process in order to simplest fit the $^5D_4$ band to the model.

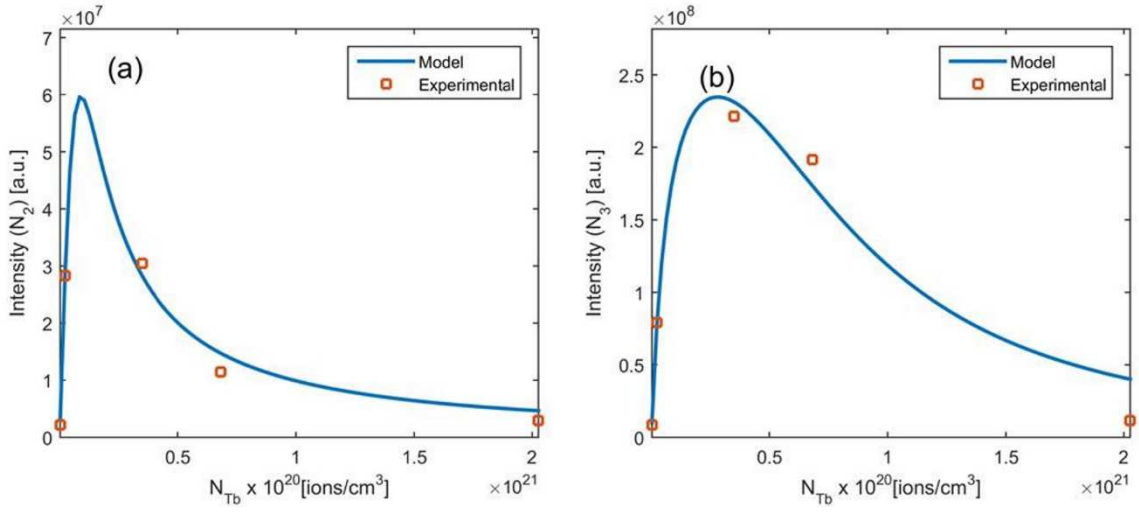

Figure 5. Integrated photoluminescent emission (red squares) vs model simulated (solid line) in $Gd_2O_2S:Tb^{3+}$ microcrystals as a function of Tb^{3+} concentration. Image a)

depicts the behavior of the emission intensity at the N_2 ($^5D_3$) level, and b) at the N_3 ($^5D_4$) level of Tb^{3+} ions.

3.4 Stationary Rate equations

In order to explain the luminescent emission and concentration quenching, we use a rate equation model in its steady state. This model represents the population density at each energy level, and the population density of each level is directly related to their emission [21]. The model represents the Gd^{3+} and Tb^{3+} populations as follows:

$$\frac{dN_1}{dt} = -A_{1b}N_1 + RN_{Gd} - W_1N_1N_{Tb} \quad (2)$$

$$\frac{dN_2}{dt} = -(A_{23} + A_{2b})N_2 + W_1N_1N_{Tb} - W_2N_2N_{Tb} \quad (3)$$

$$\frac{dN_3}{dt} = -A_{3b}N_3 + A_{23}N_2 - W_3N_3N_{Tb} \quad (4)$$

Where N_1, N_2 and N_3 (ions/cm^3) are the population densities of Gd^{3+}($^6P_{7/2}$), Tb^{3+}($^5D_3$) and Tb^{3+}($^5D_4$) energy levels, respectively (see Figure 4). N_{Gd} and N_{Tb} are the population densities in the ground state of Gd^{3+} and Tb^{3+}, respectively. The population densities in the ground state, are approximately equal to the nominal ion densities corresponding to Gd^{3+} and Tb^{3+} concentrations (see table II). A_{1b} (eq. 2) is the radiative and non-radiative relaxation from the levels Gd^{3+} ($^6P_{7/2}\rightarrow{}^8S_{7/2}$), A_{2b} (eq. 3) and A_{3b} (eq. 4) are the radiative relaxation from Tb^{3+}($^5D_3\rightarrow{}^2F_{0,\ldots,6}$) and Tb^{3+} ($^5D_4\rightarrow{}^2F_{0,\ldots,6}$), respectively. A_{23} (eq. 3) is the non-radiative relaxation from the levels Tb^{3+} ($^5D_3\rightarrow{}^5D_4$). In this model, W_1 (eq. 2, 3) is the energy transfer that occurs from Gd^{3+}($^6P_{7/2}$) → Tb^{3+}($^5H_7$), as well as a fast non-radiative relaxation to Tb^{3+}($^5D_3$). W_2 (eq. 3) and W_3 (eq. 4) represent the energy transfer responsible for the concentration quenching, from level Tb^{3+}($^5D_3$) and Tb^{3+}($^5D_4$) to another Tb^{3+} ions, after the transfer, the energy is lost, in the form of a multi-phonon emission process. R (eq. 5) is the absorption pump rate (s^{-1}) for a transition from $^8S_{7/2} \rightarrow {}^6P_{7/2}$ and can be calculated as follows [23]:

$$R = \frac{\lambda_p}{hc\pi w_p^{\,2}} P\sigma \quad (5)$$

Where P (W/cm^2) is the incident pumping power, λ_p is the pumping wavelength, w_p is the pumping radius, h is the Planck's constant, c is the vacuum speed of light, and σ

is the absorption cross section from level $^8S_{7/2}$ to level $^6P_{7/2}$. Solving the system of non-linear equations (in the steady's case), we can find the population densities N_1 (eq. 6), N_2 (eq. 7), and N_3 (eq. 8).

$$N_1 = \frac{RN_{Gd}}{A_{1a} + W_1 N_b} \tag{6}$$

$$N_2 = \frac{RW_1 N_{Gd} N_{Tb}}{\left(A_{1Tb} + W_1 N_{Tb}\right)\left(A_{23} + A_{2Tb} + W_2 N_{Tb}\right)} \tag{7}$$

$$N_3 = \frac{A_{23} W_1 R N_{Gd} N_{Tb}}{\left(A_{1Tb} + W_1 N_{Tb}\right)\left(A_{23} + A_{2Tb} + W_2 N_{Tb}\right)\left(A_{3Tb} + W_3 N_{Tb}\right)} \tag{8}$$

The population density of each level is directly related to its emission [18] by using the equations 9 to 11:

$$N_2 = k \int_{360}^{460} I(\lambda) d\lambda \tag{9}$$

$$N_3 = k \int_{475}^{600} I(\lambda) d\lambda \tag{10}$$

$$\int_{360}^{600} I\,(\lambda) d\lambda = \frac{1}{K}(N_2 + N_3) \tag{11}$$

Where k is a constant of proportionality and $I(\lambda)$ are the emission spectra as a function of wavelength λ. As we can see, in the equations from 6 to 10, there are a large number of constants that their exact value cannot be found. However, these equations show a consistent trend of the luminescent intensity that is shown as follows in the equations 12 and 13:

$$N_2 = \frac{q_1 N_{Gd} N_{Tb}}{p_1 + p_2 N_{Tb} + N_{Tb}^{\ 2}} \tag{12}$$

$$N_3 = \frac{q_2 N_{Gd} N_{Tb}}{p_3 + p_4 N_{Tb} + p_5 N_{Tb}^{\ 2} + N_{Tb}^{\ 3}} \tag{13}$$

In order to simplify the equations 7 and 8, we grouped the unknown's values by q_1, q_2, p_1, p_2, p_3, p_4 and p_5. In this way, the model has seven unknowns for ten experimental data, i.e., five measurements for the N_2 level and another five for the N_3 level. The arithmetic values of the constants are described in the supporting information. Thus, the equations 12 and 13 are in agreement with the experimental data in Figure 5. These equations explain the concentration quenching of luminescence, and additionally predict the concentration of maximum emission. We took the following values for the constants: $q_1 = 4.6177 \times 10^5 \left[\frac{ions}{cm^3}\right] k$, $q_2 = 9.3755 \times 10^{27} [\frac{ions^2}{cm^6}] k$, $p_1 = 8.1592 \times 10^{39} [\frac{ions^2}{cm^6}]$, $p_2 = 6.7501 \times 10^{11} [\frac{ions}{cm^3}]$, $p_3 = 5.0563 \times 10^{61} [\frac{ions^3}{cm^9}]$, $p_4 = 6.5717 \times 10^{41} [\frac{ions^2}{cm^6}]$, $p_5 = 2.821 \times 10^{15} [\frac{ions}{cm^3}]$. About 96% of the experimental variability of the $^5D_3$ emission is explained by this setting, depending only on Tb^{3+} concentration. For the $^5D_4$ emission, the model is set at 94%. This intensity changes with the Tb^{3+} dopant concentration, causing a color change in the emission. For high concentrations, the green emission is dominant for *N_3*, but for low concentrations, the violet-blue emission *N_2* has its maximum emission value, because much of the population in level $^5D_3$ relaxes non-radiatively to the lower $^5D_4$ level.

3.5 Color space dependence by dopant concentration

To estimate color dependence on Tb^{3+} concentration, we estimate the CIE XYZ tristimulus values X, Y, and Z. The tristimulus values of a color with a VIS emission are given in terms of the standard observer [24] by:

$$X = \int_{vis} I(\lambda)\overline{X}(\lambda)\, d\lambda \tag{14}$$

$$Y = \int_{vis} I(\lambda)\overline{Y}(\lambda)\, d\lambda \tag{15}$$

$$Z = \int_{vis} I(\lambda)\overline{Z}(\lambda)\, d\lambda \tag{16}$$

Where $\overline{X}$, $\overline{Y}$ and $\overline{Z}$ are the color-matching functions (CIE 1931), the chromaticity of a color is then specified by the two derived parameters *x* and *y*.

$$x = \frac{X}{X + Y + Z} \tag{17}$$

$$y = \frac{Y}{X + Y + Z} \tag{18}$$

Using the equations from 9 to 11, we can correlate the VIS emission spectrum as a function of the population densities in N_2 and N_3 by

$$I(\lambda) = \frac{1}{k}\left(N_2 I_2(\lambda) + N_3 I_3(\lambda)\right) \tag{19}$$

Where $I_2(\lambda)$ and $I_3(\lambda)$ are normalized spectra in the corresponding band range [18]. Substituting equation 19 in equations 17 and 18

$$x = \frac{a_1 + (N_2 / N_3)}{a_3 + a_2 (N_2 / N_3)} \tag{20}$$

$$y = \frac{a_4 + (N_2 / N_3)}{a_6 + a_5 (N_2 / N_3)} \tag{21}$$

Where (N_2 / N_3) is the rate of equations 12 and 13. The a_i (i=1 to 6) constants are obtained by color-matching functions and normalized spectra, in the corresponding band range, a_1= 2.54, a_2= 5.96, a_3= 9.03, a_4= 301.17, a_5= 343.06 and a_6= 519,87. The a_i constants are defined by the equations from 22 to 27:

$$a_1 = \frac{\int I_3(\lambda)\overline{X}(\lambda)\,d\lambda}{\int I_2(\lambda)\overline{X}(\lambda)\,d\lambda} \tag{22}$$

$$a_2 = \frac{\int I_2(\lambda)\left(\overline{X}(\lambda) + \overline{Y}(\lambda) + \overline{Z}(\lambda)\right)d\lambda}{\int I_2(\lambda)\overline{X}(\lambda)\,d\lambda} \tag{23}$$

$$a_3 = \frac{\int I_3(\lambda)\left(\overline{X}(\lambda) + \overline{Y}(\lambda) + \overline{Z}(\lambda)\right)d\lambda}{\int I_2(\lambda)\overline{X}(\lambda)\,d\lambda} \tag{24}$$

$$a_4 = \frac{\int I_3(\lambda)\overline{Y}(\lambda)\,d\lambda}{\int I_2(\lambda)\overline{Y}(\lambda)\,d\lambda} \tag{25}$$

$$a_5 = \frac{\int I_2(\lambda)\left(\overline{X}(\lambda)+\overline{Y}(\lambda)+\overline{Z}(\lambda)\right)d\lambda}{\int I_2(\lambda)\overline{Y}(\lambda)\,d\lambda} \tag{26}$$

$$a_6 = \frac{\int I_3(\lambda)\left(\overline{X}(\lambda)+\overline{Y}(\lambda)+\overline{Z}(\lambda)\right)d\lambda}{\int I_2(\lambda)\overline{Y}(\lambda)\,d\lambda} \tag{27}$$

Figure 6 shows the experimental color coordinates, where green color is dominant. Table III shows the experimental and the simulation of equations 20 and 21. It is important to emphasize that luminescent intensity and color coordinates are only explained by the effect of traps, i.e. Tb^{3+} ions migrate through a large number of Tb^{3+} ions before being emitted. However, even for the purest crystals, these centers can relax to their ground state by multiphonon emission, and inhibit the luminescence. Additionally, the proposed algebraic equations (20 and 21), can be used to explain the visible emission to other systems by doping them with ions of Gd^{3+} and Tb^{3+}.

Table III. Experimental (X_e *and* Y_e) and model simulated (X_m *and* Y_m) for color coordinates

CIE 1931	Tb^{3+} Concentration				
Coordinates	0,01	0,1	1,3	3,0	9,0
x_m	0,266	0,260	0,272	0,277	0,265
x_e	0,277	0,255	0,278	0,287	0,267
y_m	0,503	0,472	0,532	0,558	0,499
y_e	0,457	0,486	0,547	0,577	0,496

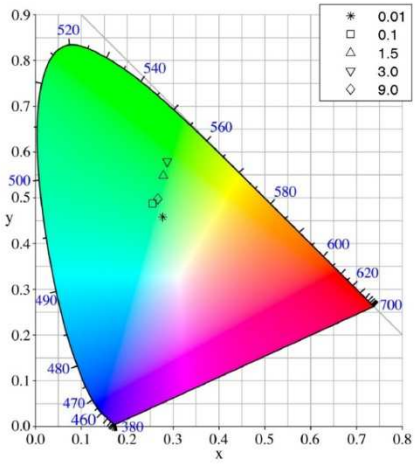

Figure 6. CIE 1931 color space chromaticity diagram for $Gd_2O_2S:Tb^{3+}$ microcrystals with different dopant concentrations.

3.6 Temperature effect on the luminescent emission

According to the model, the only temperature-dependent parameters are the radiative and non-radiative relaxations represented by A_{1b} (eq. 2), A_{2b} (eq. 3), A_{3b} (eq. 4), and A_{23} (eq. 4), respectively. There

$$A_{1b} = A_{1b}^{rad} + A_{1b}^{mp} \quad (28)$$

$$A_{2b} = A_{2b}^{rad} + A_{2b}^{mp} \quad (29)$$

$$A_{3b} = A_{3b}^{rad} + A_{3b}^{mp} \quad (30)$$

Where $A_{1b,2b,3b}^{rad}$ are the photon rate and $A_{1b,2b,3b}^{mp}$ are the multi-phonon rate. In the case of the A_{23}, this parameter only has a multi-phonon rate part (the non-radiative relaxation from the levels Tb^{3+} ($^5D_3 \rightarrow {}^5D_4$)). In general, an increase in the temperature of the sample will produce a substantial increase in the multi-phonon rate emission [25, 26]. In this way, the values of q2, and from p1 to p5 will increase with the trend of the increase in temperature and therefore the emission intensities will be reduced when the temperature is increased (see equations 12 and 13).

Conclusions

We analyzed the luminescent emission and color tonality in the Gd_2O_2S matrix as a function of Tb^{3+} concentration by comparing experimental data and a rate equations

model. The set of the algebraic equations, explains satisfactorily the behavior of the emission intensity and modulation of color from red to blue in $Gd_2O_2S:Tb^{3+}$ microcrystals. The mechanism of quenching traps was found to be the main route for the emission intensity and color tonality due to the cross-relaxation process at high Tb^{3+} concentrations is not satisfactory according to the experimental results. Moreover, for high concentrations, the green emission is dominant for the $^5D_4$ level of Tb^{3+}, but for low concentrations, the violet-blue emission $^5D_3$ has its maximum emission value, because much of the population in this level relaxes non-radiatively to the lower $^5D_4$ level. These results helped us to understand and simulate the intensity of the emission bands in $Gd_2O_2S:Tb^{3+}$, which is undoubtedly an important feature in the development of luminescent materials for technological and medical applications.

Acknowledgments

LHA thanks CONACYT (Mexico) for his postdoctoral support (Grant number 252064). PLHA thanks CONACYT for his doctoral grant (Grant number 429285). We acknowledge Claudia G. Elias Alfaro for TEM technical support and Dr. John Eder Sanchez from the UASLP for his valuable comments.

References

[1] A. Szczeszak, A. Ekner-Grzyb, M. Runowski, K. Szutkowski, L. Mrówczyńska, Z. Kaźmierczak, T. Grzyb, K. Dąbrowska, M. Giersig, S. Lis, Spectroscopic, structural and in vitro cytotoxicity evaluation of luminescent, lanthanide doped core@shell nanomaterials $GdVO_4:Eu^{3+}@SiO_2@NH_2$, Journal of Colloid and Interface Science. 481 (2016) 245–255. doi:10.1016/j.jcis.2016.07.025.

[2] L. Hernandez-Adame, N. Cortez-Espinosa, D.P. Portales-Pérez, C. Castillo, W. Zhao, Z.N. Juarez, L.R. Hernandez, H. Bach, G. Palestino, Toxicity evaluation of high-fluorescent rare-earth metal nanoparticles for bioimaging applications, J. Biomed. Mater. Res. 105 (2017) 605–615. doi:10.1002/jbm.b.33577.

[3] P. Pust, P.J. Schmidt, W. Schnick, A revolution in lighting, Nat Mater. 14 (2015) 454–458.

[4] K. Zarschler, L. Rocks, N. Licciardello, L. Boselli, E. Polo, K.P. Garcia, L. De Cola, H. Stephan, K.A. Dawson, Ultrasmall inorganic nanoparticles: State-of-the-art and perspectives for biomedical applications, Nanomedicine: Nanotechnology, Biology and Medicine. 12 (2016) 1663–1701. doi:10.1016/j.nano.2016.02.019.

[5] S.A. Osseni, S. Lechevallier, M. Verelst, P. Perriat, J. Dexpert-Ghys, D. Neumeyer, R. Garcia, F. Mayer, K. Djanashvili, J.A. Peters, E. Magdeleine, H. Gros-Dagnac, P. Celsis, R. Mauricot, Gadolinium oxysulfide nanoparticles as multimodal imaging agents for T2-weighted MR, X-ray tomography and photoluminescence, Nanoscale. 6 (2014) 555–564. doi:10.1039/C3NR03982J.

[6] A. Cabrera-García, A. Vidal-Moya, Á. Bernabeu, J. Pacheco-Torres, E. Checa-Chavarria, E. Fernández, P. Botella, Gd-Si Oxide Nanoparticles as Contrast Agents in Magnetic Resonance Imaging, Nanomaterials (Basel). 6 (2016). doi:10.3390/nano6060109.

[7] M.W. Ahmad, W. Xu, S.J. Kim, J.S. Baeck, Y. Chang, J.E. Bae, K.S. Chae, J.A. Park, T.J. Kim, G.H. Lee, Potential dual imaging nanoparticle: Gd_2O_3 nanoparticle, Scientific Reports. 5 (2015) srep08549. doi:10.1038/srep08549.

[8] S.-M. Hsiao, B.-Y. Peng, Y.S. Tseng, H.-T. Liu, C.-H. Chen, H.-M. Lin, Preparation and characterization of multifunctional mesoporous silica nanoparticles for dual magnetic resonance and fluorescence imaging in targeted cancer therapy, Microporous and Mesoporous Materials. 250 (2017) 210–220. doi:10.1016/j.micromeso.2017.04.050.

[9] L. Hernández-Adame, A. Méndez-Blas, J. Ruiz-García, J.R. Vega-Acosta, F.J. Medellín-Rodríguez, G. Palestino, Synthesis, characterization, and photoluminescence properties of Gd:Tb oxysulfide colloidal particles, Chemical Engineering Journal. 258 (2014) 136–145. doi:10.1016/j.cej.2014.07.067.

[10] P. Padhye, A. Alam, S. Ghorai, S. Chattopadhyay, P. Poddar, Doxorubicin-conjugated β-$NaYF_4$:Gd^{3+}/Tb^{3+} multifunctional, phosphor nanorods: a multi-modal, luminescent, magnetic probe for simultaneous optical and magnetic resonance imaging and an excellent pH-triggered anti-cancer drug delivery nanovehicle, Nanoscale. 7 (2015) 19501–19518. doi:10.1039/C5NR04473A.

[11] A.A. da Silva, M.A. Cebim, M.R. Davolos, Excitation mechanisms and effects of dopant concentration in Gd_2O_2S:Tb^{3+} phosphor, Journal of Luminescence. 128 (2008) 1165–1168. doi:10.1016/j.jlumin.2007.11.095.

[12] S.-L. Lin, T.-Y. Liu, C.-L. Lo, B.-S. Wang, Y.-J. Lee, K.-Y. Lin, C.A. Chang, Synthesis, surface modification, and photophysical studies of Ln_2O_2S:Ln^{3+} (Ln=Gd, Tb, Eu; Ln′=Tb and/ or Eu) nanoparticles for luminescence bioimaging, Journal of Luminescence. 175 (2016) 165–175. doi:10.1016/j.jlumin.2016.01.037.

[13] Y. Waseda, E. Matsubara, K. Shinoda, X-Ray Diffraction Crystallography, Springer Berlin Heidelberg, Berlin, Heidelberg, 2011. doi:10.1007/978-3-642-16635-8.

[14] M.D. Faucher, R. Morlotti, O.K. Moune, The effects of added foreign ions in Gd_2O_2S:Tb^{3+}; crystal field calculations, lifetimes, photo-luminescence and absorption spectra, Journal of Luminescence. 96 (2002) 37–49. doi:10.1016/S0022-2313(01)00212-5.

[15] M.A. Cebim, A.A.D. Silva, M.R. Davolos, Spectroscopy properties and energy level location of Gd_2O_2S:Pr^{3+},Ce^{3+}, Phys. Status Solidi (C). 6 (2009) S171–S174. doi:10.1002/pssc.200881284.

[16] J. Lü, T. Fan, J. Xie, G. Chen, Tunable luminescence and energy transfer of $TbPO_4$:Eu^{3+} nanocrystals, Optics Communications. 286 (2013) 221–223. doi:10.1016/j.optcom.2012.08.093.

[17] Z. Xia, R.-S. Liu, Tunable Blue-Green Color Emission and Energy Transfer of $Ca_2Al_3O_6F$:Ce^{3+},Tb^{3+} Phosphors for Near-UV White LEDs, J. Phys. Chem. C. 116 (2012) 15604–15609. doi:10.1021/jp304722z.

[18] O. Meza, L.A. Diaz-Torres, P. Salas, E. De la Rosa, D. Solis., Color tunability of the upconversion emission in Er–Yb doped the wide band gap nanophosphors ZrO_2 and Y_2O_3, Materials Science and Engineering: B. 174 (2010) 177–181. doi:10.1016/j.mseb.2010.03.015.

[19] T. Tsuji, Y. Terai, M.H.B. Kamarudin, K. Yoshida, Y. Fujiwara, Concentration quenching in Eu-doped ZnO grown by sputtering-assisted metalorganic chemical vapor deposition, Journal of Luminescence. 132 (2012) 3125–3128. doi:10.1016/j.jlumin.2011.12.042.

[20] J.G. Solé, L.E. Bausá, D. Jaque, Applications: Rare Earth and Transition Metal Ions, and Color Centers, in: An Introduction to the Optical Spectroscopy of Inorganic Solids, John Wiley & Sons, Ltd, 2005: pp. 199–234. doi:10.1002/0470016043.ch6.

[21] P.A. Tanner, Spectra, Energy Levels and Energy Transfer in High Symmetry Lanthanide Compounds, in: H. Yersin (Ed.), Transition Metal and Rare Earth Compounds: Excited States, Transitions, Interactions III, Springer Berlin Heidelberg, Berlin, Heidelberg, 2004: pp. 167–278. doi:10.1007/b96863.

[22] K. L. Bray, Luminescent Materials By G. Blasse (University of Utrecht, The Netherlands) and B. C. Grabmaier (Siemens Research Laboratories). Springer. Journal of the American Chemical Society, 1996: 118(42), 10340. doi:10.1021/ja965667t

[23] H. Yersin, Triplet Emitters for OLED Applications. Mechanisms of Exciton Trapping and Control of Emission Properties, in: H. Yersin (Ed.), Transition Metal and Rare Earth Compounds: Excited States, Transitions, Interactions III, Springer Berlin Heidelberg, Berlin, Heidelberg, 2004: pp. 1–26. doi:10.1007/b96858.

[24] N. Ohta, A.R. Robertson, Evolution of CIE Standard Colorimetric System, in: Colorimetry, John Wiley & Sons, Ltd, 2005: pp. 175–228. doi:10.1002/0470094745.ch6.

[25] C. Reber, H. U. Güdel, Nonradiative relaxation processes in V^{3+} doped halide and oxide lattices, Journal of Luminescence. 47 (1990) 7-18. doi: 10.1016/0022-2313(90)90053-E

[26] C. W. Struck, W.H. Fonger, Unified model of the temperature quenching of narrow-line and broad-band emissions, Journal of Luminescence. 10 (1975) 1-30. doi: 10.1016/0022-2313(75)90029-0.

Highlights

- The rate equation model can simulate the visible emission and concentration quenching of luminescence
- The mechanism of quenching traps was found the main route that affect the emission intensity and color tonality
- For high Tb^{3+} concentrations, the green emission has its maximum level, but for low concentrations, the violet-blue emission is dominant.